

PCCP

Accepted Manuscript



This is an *Accepted Manuscript*, which has been through the Royal Society of Chemistry peer review process and has been accepted for publication.

Accepted Manuscripts are published online shortly after acceptance, before technical editing, formatting and proof reading. Using this free service, authors can make their results available to the community, in citable form, before we publish the edited article. We will replace this *Accepted Manuscript* with the edited and formatted *Advance Article* as soon as it is available.

You can find more information about *Accepted Manuscripts* in the [Information for Authors](#).

Please note that technical editing may introduce minor changes to the text and/or graphics, which may alter content. The journal's standard [Terms & Conditions](#) and the [Ethical guidelines](#) still apply. In no event shall the Royal Society of Chemistry be held responsible for any errors or omissions in this *Accepted Manuscript* or any consequences arising from the use of any information it contains.

Near Field Plasmonic Gradient Effects on High Vacuum Tip-enhanced Raman Spectroscopy

Yurui Fang,^{1,2,†} Zhenglong Zhang,^{3,†} Li Chen,^{1,4} Mengtao Sun^{1,*}

1. *Beijing National Laboratory for Condensed Matter Physics, Institute of Physics, Chinese Academy of Sciences, P. O. Box 603-146, Beijing, 100190, People's Republic of China*
2. *Division of Bionanophotonics, Department of Applied Physics, Chalmers University of Technology, Gothenburg SE-412 96, Sweden*
3. *Leibniz Institute of Photonic Technology, Albert-Einstein-Str. 9, 07745 Jena, Germany*
4. *Department of Electrical and Computer Engineering, University of California, San Diego, 9500 Gilman Drive, La Jolla, California 92093, USA*

† Contributed Equally.

* Corresponding author, Email: mtsun@iphy.ac.cn (M. T. Sun).

Abstracts

The near field gradient effects in high vacuum tip-enhanced Raman spectroscopy (HV-TERS) is a latest developing ultra-sensitive optical and spectral analysis technology in nanoscale, based on the plasmons and plasmonic gradient enhancement in near field and in high vacuum. Using HV-TERS, it can not only be used to detect ultra-sensitive Raman spectra by surface plasmon enhancement, but also to detect clear molecular IR-active modes by strongly enhanced plasmonic gradient. Furthermore, the molecular overtone modes and combinational modes can also be experimentally measured, where the Fermi resonance and Darling-Dennison resonance were successfully observed in HV-TERS. Theoretical calculations using electromagnetic field theory firmly supported experimental observation. The intensity ratio of plasmon gradient term over linear plasmon term can reach up to larger than 1. Theoretical calculations also revealed that with the increase of gap distance between tip and substrate, the decrease of plasmon gradient is significantly quickly than the decrease of plasmon intensity, which is the reason that the gradient Raman can be only observed in near field. Recent experimental results about near field gradient effects on HV-TERS were summarized, following the section of the theoretical analysis.

I. Introduction

Tip-enhanced Raman spectroscopy (TERS), combining of Raman spectroscopy and scanning probe microscopy techniques, has been one of promising ultrasensitive spectral analysis technology in the nano science and technology, because of high-sensitivity and high spatial-resolution beyond the diffraction limit of light.¹⁻⁴⁶ The use of high vacuum (HV) is mandatory for the spectral measurements that molecules are sensitive to ambient conditions.^{2-4, 8-11, 21, 22, 37, 38, 45, 46} The scanning tunneling microscopy (STM) based HV-TERS can provide atomic-resolution STM imaging and structural elucidation of adsorbed specimens on clean, single-crystal surfaces at low temperature, or localized spectroscopic information of surface-catalyzed reactions^{21, 33, 47} There are several excellent review papers on TERS.^{1, 7, 23, 24, 31, 32, 42, 43} In the latest development of home-made HV-STM-TERS, the object (50 \times , NA = 0.5) is put into the HV chamber and near the tip/substrate about 10.5 mm (see Scheme one),^{30, 37} so that the efficiency of collecting Raman signals can be significantly improved to simultaneously measure Stokes and anti-Stokes HV-TER spectra. Furthermore, the temperature near the nano gap between tip and substrate can be in situ obtained, combining the measured Stokes and anti-Stokes HV-TER spectra.³⁷

The plasmon gradient effect was firstly investigated by Ayars and Hallen in 2000,^{48, 49} however, it is still a largely unexplored territory in TERS before the year of 2013, while it is a very important issue and urgent being physically understood. Thanks to TERS, which is mainly applied in combination with linear optical processes in Raman, the near field gradient effects are becoming a blossoming topic since the year of 2013, because not only the molecular IR-active modes can be observed, but also the higher-order Raman, such as overtone modes or the combinational modes, can also be observed experimentally.^{3, 4, 10, 45, 46} These investigations can reveal the significant difference between near field Raman and far field Raman. The more vibrational information provides, the more convincing evidence can be obtained for chemical analysis on the nanoscale. Physical understanding of the contributions of near field gradient effect on TERS is mandatory.

The Hamiltonian for Raman spectra of a molecule in an inhomogeneous

electromagnetic field can be written as,^{50, 51}

$$H = H_0 + H_1 + H_2$$

$$= \left(\alpha_{\alpha\beta} E_\beta + \frac{1}{3} A_{\alpha,\beta\gamma} \frac{\partial E_{\beta\gamma}}{\partial r} \right) E_\alpha + \frac{1}{3} \left(A_{\gamma,\alpha\beta} E_\gamma + C_{\alpha\beta,\gamma\delta} \frac{\partial E_{\gamma\delta}}{\partial r} \right) \frac{\partial E_{\alpha\beta}}{\partial r} + \dots \quad (1)$$

where $\alpha_{\alpha\beta}$, $A_{\alpha,\beta\gamma}$ and $C_{\alpha\beta,\gamma\delta}$ are the electric dipole-dipole, dipole-quadrupole and quadrupole-quadrupole interaction coefficient. E_α is the external electric field and $\frac{\partial E_{\alpha,\beta\gamma}}{\partial r}$ is the electric field gradient, which can result in the activation of molecular IR modes or overtone modes.^{3, 4, 10, 45, 46} The Fermi resonance^{45, 52} and Darling-Dennison resonance^{46, 53} in the observations of overtone modes were successfully observed in HV-TERS.

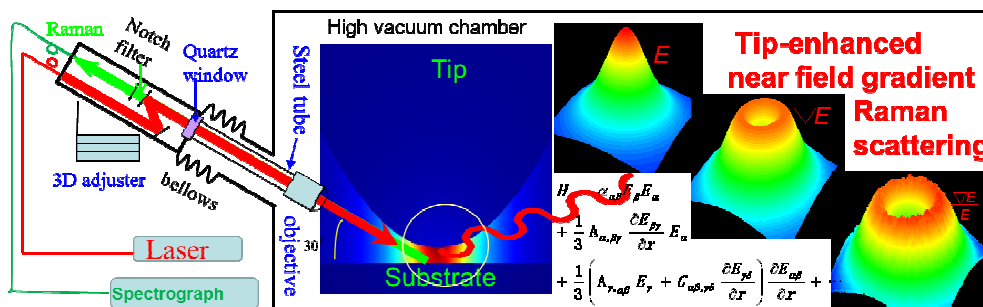


Fig 1. The scheme of HV-TERS setup, and the near field gradient effects on HV-TERS, which is taken from Ref. [4].

The intensity of vibrational modes can be written as,^{50, 51, 54}

$$I = I_1 + I_2 + \dots$$

$$= \langle j | H_0 | i \rangle^2 + 4 \langle j | H_0 | i \rangle \langle j | H_1 | i \rangle + \dots \quad (2)$$

where Raman shift is ignored, and $H_1 = H_2$ omitted. So, the Intensity ratio of IR-active mode over Raman modes can be

$$\frac{I_2}{I_1} = 4 \times \frac{1}{3} \sum_{\alpha\beta\gamma} \frac{A_{\alpha,\beta\gamma}}{\alpha_{\alpha\beta}} \times \frac{\nabla E_{\beta\gamma}}{E_\beta} \quad (3)$$

Where $\frac{A_{\alpha,\beta\gamma}}{\alpha_{\alpha\beta}}$ and $\frac{\nabla E_{\beta\gamma}}{E_\beta}$ are contributed from molecular and plasmon properties in TERS, respectively. If we just consider the plasmon terms determined by the TERS

system, then

$$\frac{I_2}{I_1} \propto 4 \times \frac{\nabla E_{\beta\gamma}}{E_{\beta}} \quad (4)$$

In this review, we focus on the contribution of the electric field gradient terms in Eq.(1) to the TER spectra in the near field. Fig. 1 demonstrates the main point of the near field gradient effects in HV-TERS with our home-made setup. The content is arranged as follow: **First**, the home-made HV-STM-TERS setup was introduced. **Second**, the parameters dependent surface plasmon resonance (SPR) spectra was proposed to optimize the suitable tip size for best SPR at the incident light wavelength, where the substrate is considered as a smooth surface for simplification. Furthermore, we reveal the near field gradient Raman in the case of roughness substrate in TERS, which proved that the roughness of substrate can significantly increase the contribution of near field gradient Raman in TERS. **Third**, we review recent experimental works on near field gradient Raman on the HV-TERS. **Last**, we close the review with conclusion and prospective.

II. Setup of home-made HV-TERS

The schematic diagram of the home-made HV-TERS system is shown in Fig. 2.³⁰ It consists of a Molecular beam epitaxy (MBE) chamber, a fast loading chamber and an analyzing chamber which contains a homemade scanning tunneling microscope (STM) and a Raman spectrometer. In the MBE chamber there are an Ar⁺ gun for cleaning surfaces, two replaceable metal sources for making different films and two replaceable molecule sources for depositing target molecules on substrate. Single crystal metal film could be prepared and monolayer molecules could be deposited in this chamber. In the fast loading chamber one could either load sample prepared outside or transfer samples prepared in MBE chamber to the analyzing chamber. In the analyzing chamber there is a STM for imaging the samples in atomic resolution. Combining with the STM, an objective is used to focus laser to the STM tip and collect signals from the tip-substrate gap. A 3D adjustable stage is used for focusing. The three chambers are separated with

gate valves so as to be use separately without losing the vacuum when opening the others. The inset of Fig.2 shows the scheme of the basic idea of our HV-TERS.

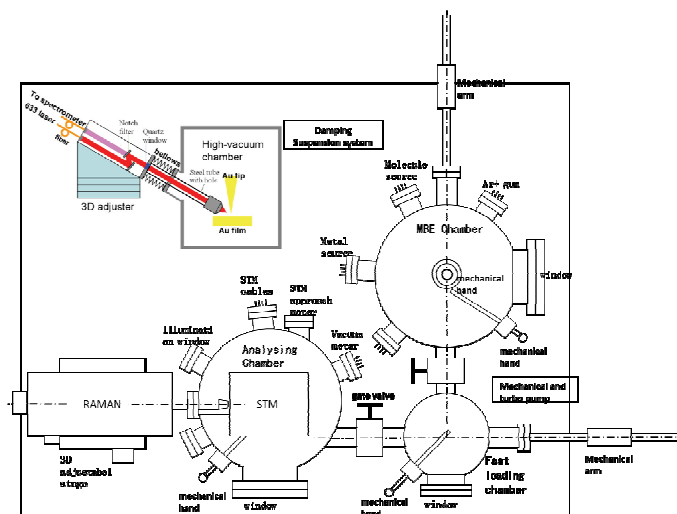


Figure 2. Scheme of the HV-TERS system with a preparing MBE chamber, a fast loading chamber and a TERS Analysis chamber.

Based on the scheme, the drawings with exact accurate demotions and details were designed with commercial software Solid Works and the instrument was produced with cooperation of several companies. Fig. 3 shows the picture of the real finished instrument.¹⁹ Fig. 3a shows a whole view of the instrument. Each chamber has an ion pump and there is an extra Ti sublimation pump for the analyzing chamber because it is bigger and has more components in the chamber. The pressure in the chambers is about 10^{-7} Pa. The high vacuum guarantees the experiment in a pure environment, which reduces the contamination of the samples and makes the STM tip-substrate gap in a pure tunneling state. Fig. 3b shows the objective and STM tip when the laser was focused on the tip and the tip image from the objective is shown in Fig. 3c. The Raman optical components and 3D adjustable stage are put outside of the chamber but the objective is put inside of the chamber. There are holes in the objective and the objective tube for releasing gas when they are put in the high vacuum chamber. The objective was connected to the outside parts with the tube and the chamber is sealed with a quartz window in the light path. A bellows tube is used to make the tube movable in 3D. The

Raman system is with side illumination of 632.8 nm He-Ne laser light with an angle of 60° off tip axis, and three-dimensional piezo stages for the tip and sample manipulations. Fig. 3d shows the MBE part in the MBE chamber with an Ar^+ gun and annealing system. Fig. 3e shows the debugging results of the HV-TERS system. Atomic resolved image and a tip-enhanced Raman spectrum were successfully obtained. The specified parameters of the setup are shown in Table 1.

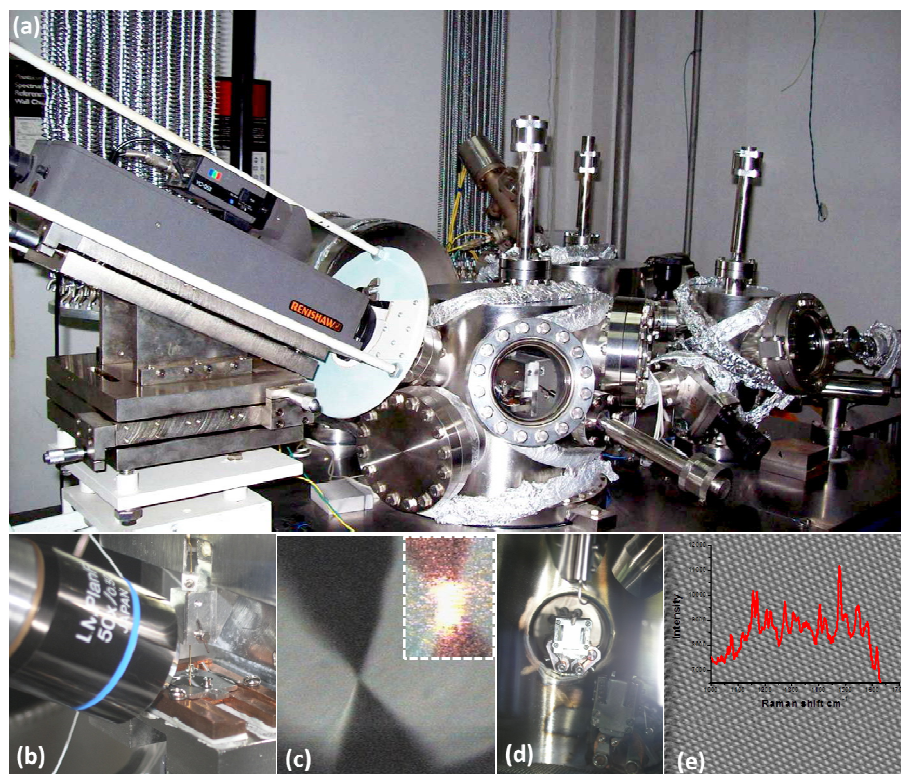


Figure 3. (a) Picture of the actual finished HV-TERS system. (b) The core part of TERS-objective and STM tip. (c) Image of the tip and the reflected tip by the substrate. The inset is when tip was illuminated with a 633nm laser. (d) the Ar^+ gun cleaning and MBE part in the MBE chamber. (e) The atomic resolved image of graphite ($7 \times 7 \text{nm}^2$). The inset is a Raman spectrum from a sample with PATP molecules on Au surface.

configuration	Vacuum	Tip	laser	STM Spatial resolution	Raman spatial resolution	Specialization	Specialization samples
Side illumination, 60° off tip axis	10 ⁻⁷ Pa	Au tip with 25nm tip radius	632.8 nm	0.1nm	30nm	Objective inside the vacuum chamber	In situ measurement

Table 1. Parameters of the home-built HV-TERS setup.

III. Theory of HV-TERS

3.1 wavelength dependent surface plasmon resonance in TERS

To obtain optimized experimental measurements in TERS, the strongest linear (the first term in Eq. (1)) and nonlinear field term (higher term in Eq.(1)) must be strongest simultaneously. According to our experimental setup, theoretical model Fig 4a in calculations was adopted, where the angle between incident light and the tip is set $\theta = 60^\circ$, d is the distance between the substrate and the tip, R is tip's radius. The substrate and the tip are Ag and Au, respectively.

Fig. 4b shows the wavelength dependent SPRs response with different gap d , where $R = 30$ nm is set. Two strong distinct SPRs peaks around 860 nm and 620 nm decreased significantly with the increase of d , while the shifts of these two SPR peaks is little. When $d = 1$ nm, plasmon enhancement of STM-TERS ($|E|^2/|E_0|^2$) is about 4×10^7 , at the incident wavelength of 632.8 nm. Fig.4c reveals that these two plasmon peaks shown in Fig. 4b decreased significantly with d increasing. However, the SPR peak at high energy is decreasing much quicker than the SPR peak at low energy. These two SPR peaks are hardly undistinguished when the gap distance is large enough (see Fig. 4d), which reveals that these two SPR peaks shown in Fig. 4b must be contributed by strong couplings between substrate and tip, and this phenomenon can be explained using hybridization theory of plasmonic nano-structures³⁵ of TERS (shown from Fig. 4e). The

energy difference of two SPR peaks (Δ) is decreasing while d is increasing (stronger coupling of the substrate and tip results in these two plasmonic peaks splitting shown in Fig. 4c and 4d).

Setting $d = 2$ nm, the SPR peak at 620 nm is blue shifted slightly, and the intensity of plasmonic peak also slightly increases, when the tip radius R increases (see Fig. 4f); but the SPR peak at 860 nm keeps un-shifted, while the intensity of SPR strongly decreases. The blue shift of SPR peak at 620 nm is resulted from the increasing of energy difference Δ shown in Fig. 4e, when tip radius R is increases, while the hybridization increases when the tip radius increases.

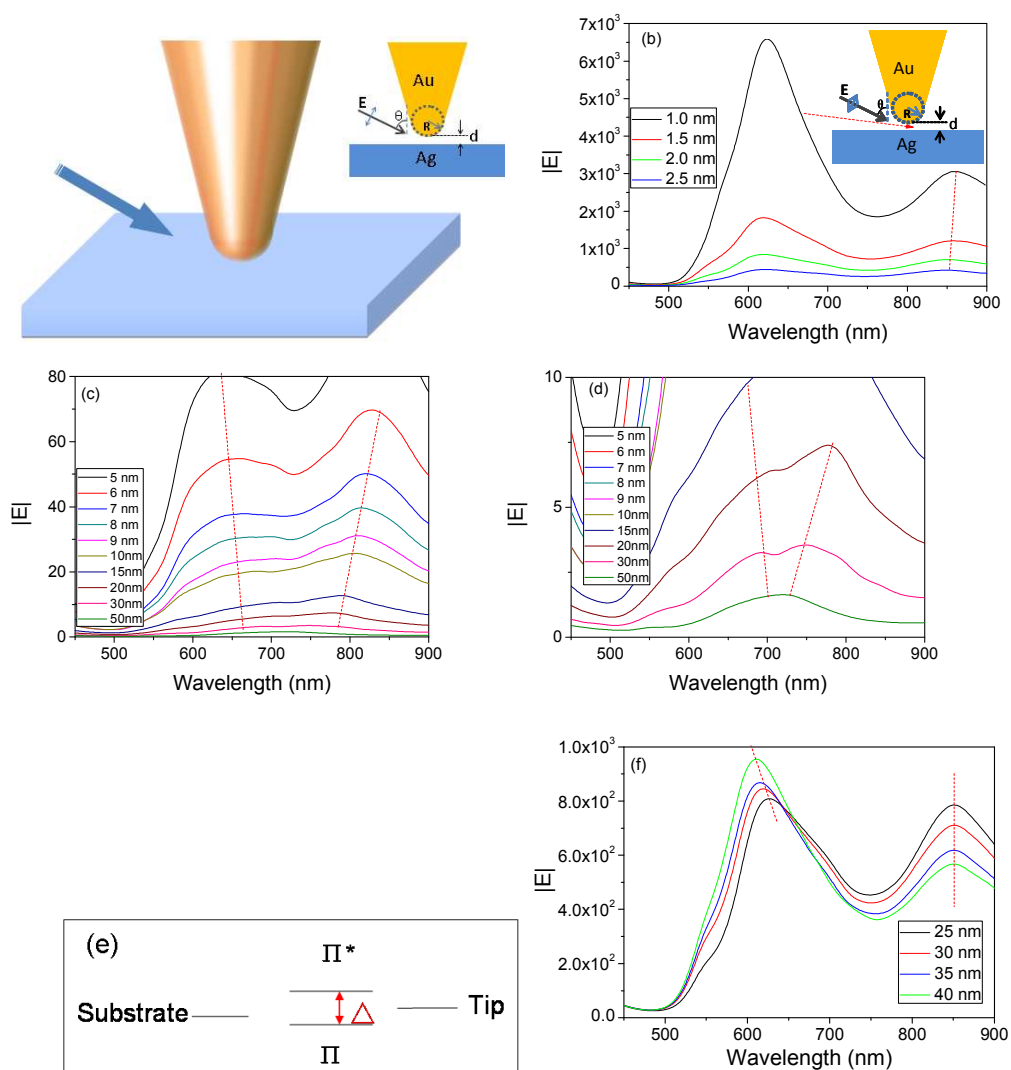


Figure 4. (a) The theoretical model for the TERS. (b)-(d) The distance dependent SPRs, (e) SPR hybridization model of TERS. (f) Tip radius dependent plasmonic peaks. Figure 4 is taken from Ref. [46].

3. 2 Near Field gradient effect on TERS at rough substrate

When molecules adsorbed on rough substrate prepared with the method of thermal vapor, semispherical shape can be set on substrates under the tip for the simulation (see Fig. 5a).³

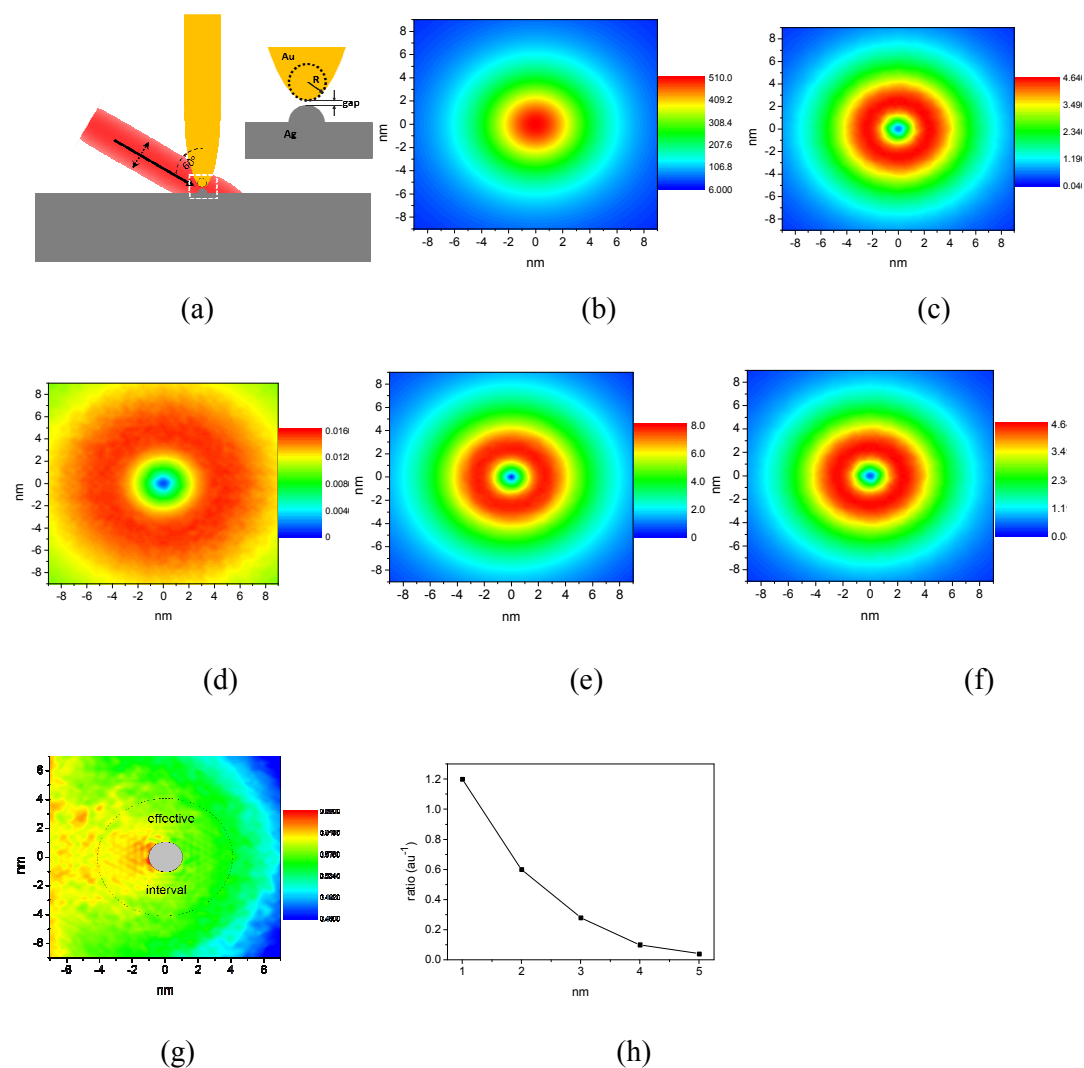


Figure 5 . The model and the simulated electric field as well as electric field gradient effects in TERS. (a) The theoretical TERS model. (b) The distribution of electric field intensity along tip axis. (c) The intensity of electric field gradient along the tip axis (z

axis). (d) Ratio of intensity of electric field gradient over that of electric field (0.5 nm above substrate). (e) The intensity of electric field along substrate (0.5 nm above the substrate). (f) The intensity of electric field gradient along the substrate (0.5 nm above the substrate). Units of intensities of electric field and electric field gradient are V/m and V/m/au, respectively, where au is atomic unit. Figure 5 is taken from Ref. [3].

Fig. 5b shows the distribution of electric field intensity at the center of nano gap along tip axis. It clearly shows that the strongest intensity of electric field is located on the area of 27 nm^2 , where $r \sim 3.0 \text{ nm}$. Fig. 5c is the intensity of electric field gradient, which is distributed along tip axis at nano gap center. It is shown that the strongest intensity of electric field gradient is in the region of $1.0 \text{ nm} < r < 4.0 \text{ nm}$. Fig. 5d reveals the ratio of intensity of electric field gradient over that of electric field at the center of nano gap along the tip axis, which is only about 1/100; even when the third term in Eq. (1) is considered, it is 1/50. Fig. 5e is the electric field intensity distribution in the center of nano gap along the substrate, where the component of intensity of the electric field along the tip excluded. It shows that the regions of strongest intensity of electric field are within the radius of $1.0 \text{ nm} < r < 4.0 \text{ nm}$. But, the intensity of electric field in $r < 1.0 \text{ nm}$ is very weak shown in Fig. 5e. Also, the varying tendency of intensity of electric field gradient is quite similar with the intensity of electric field along the substrate (Fig. 5f). Fig. 5g demonstrates the ratio of intensities of electric field gradient over that of electric field (the second term was considered in Eq. (1) for electric field gradient), then one can find that the ratio is 0.6 in atomic unit. So the most effective interval is within $1.0 \text{ nm} < r < 4.0 \text{ nm}$ for contributions of the electric field gradient. It should be noticed that when the higher terms (the third term in Eq. 1) is also considered, the ratio $\frac{\partial E_{\beta r}}{\partial r} / E_{\beta}$ can further

increase. If $C_{\alpha\beta,\gamma\delta}$ in the fourth term is large enough, the ratio of $\frac{\partial E_{\beta\gamma}}{\partial r} \frac{\partial E_{\alpha\beta}}{\partial r} / E_{\beta} E_{\alpha}$ can reach up to 0.36. Fig. 5h demonstrates the distance dependent ratio of $\frac{\partial E_{\beta\gamma}}{\partial r} / E_{\beta}$, when the second term and the third term are considered. It is shown that the ratio significantly decreases with the increasing of gap distance. When the distance of gap is beyond 5 nm, the effect of near field gradient can be ignored. The intensity of electric field gradient along the tip axis should be the same as that on the flat surface, due to the Laplace's equation,^{3,4}

$$\frac{\partial E_{xx}}{\partial r_{xx}} + \frac{\partial E_{yy}}{\partial r_{yy}} + \frac{\partial E_{zz}}{\partial r_{zz}} = 0 \quad (5)$$

IV. Experimental reports on HV-TERS

4.1 Fundamental IR-active modes in HV-TERS

In the study the surface catalytic reaction of DMAB produced from PATP in HV-TERS, the IR-active modes of DMAB were clearly observed because of the strong gradient effect.⁴⁵ In measurements, molecular monolayer of PATP adsorbed on the gold film were measured, using the gold tip HV-TERS system, where ± 1 V bias were applied on the sample and with reference current of 1 nA. Two typical spectra at different biases are shown in Fig. 6a and 6b. The Raman and IR spectra for DMAB molecule are also obtained from calculation (Fig 6c, 6d). Comparing Fig 6a and 6b with the Raman spectrum in Fig. 6c, all Raman-active symmetric ag modes in Fig. 6a and 6b can be well assigned. But surprisingly, most of the remaining vibrational peaks in the Fig. 6a and 6b can be assigned as bu modes (IR-active asymmetric), compared with the simulated IR spectrum shown in Fig.6d. The activation of these IR modes in the Raman measurement is attributed to higher field gradients shown in Fig. 5. Furthermore, enormous electromagnetic field gradients results in the activation of IR-active modes much easy observable.

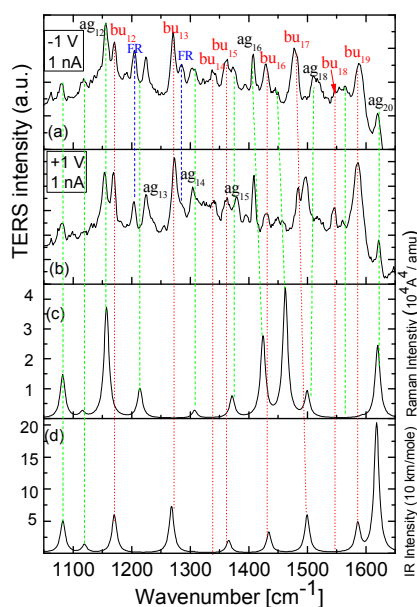


Figure 6. (a, b) TERS spectra of DMAB (± 1 V bias, 1 nA current) measured at different positions. (c) The calculated Raman spectrum and (d) IR spectrum of DMAB. Figure 6 is taken from Ref. [45].

The second example is the observation of IR-active modes of 2,2'-diamino-dimercaptoazobenzene (2,2'-DA-DMAB) produced from 2,4-dinitrobenzenethiol (2,4-DNBT) assisted by surface plasmon revealed by HV-TERS.³ Comparing spectrum of at the tunneling current of 2 nA to the spectrum of 1 nA, six IR-active vibrational peaks (the red dishes line in Fig. 7) significantly increase. With the increasing of tunneling current, the Raman peaks, especially for the three distinct Raman peaks at 1302, 1408 and 1479 cm^{-1} relatively decrease. That is because the tunneling current determines the distance between the tip and the substrate, which controlled the ratio of electric field gradient and electric field, and moreover, affected the intensities of IR-active modes over those of Raman-active modes. With the decrease of the gap distance, the ratio is significantly increased, which is because the near field gradient effect is stronger. Theoretical calculations have revealed the relationship between the ratio and the gap distance (Fig. 5h), which is consistent with the experimental results.

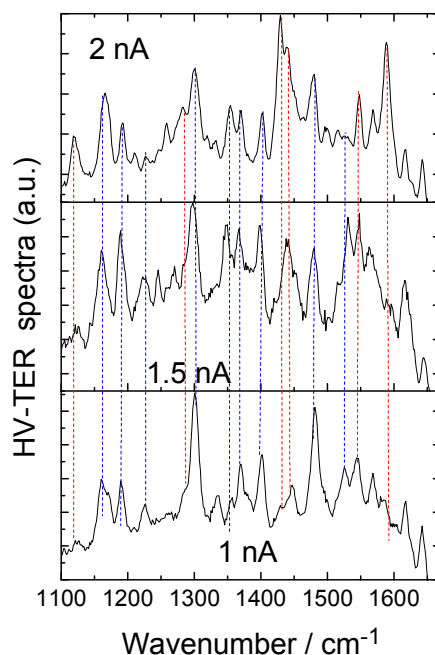


Figure 7. The tunneling current intensity dependent TER spectra of 2,2' DA-DMAB produced from 2,4-DNBT. Figure 7 is taken from Ref. [3].

The third example is the near field HV-TERS of pyrazine.⁴ The measured Raman and IR spectra of pyrazine powder and the HV-TER spectrum of pyrazine adsorbed on the Ag film were shown in Fig. 8. It reveals that HV-TER spectrum is significantly different from the normal Raman. Almost all Raman peaks of pyrazine powder can be well observed in HV-TERS, but there are many “additional” strongly enhanced vibration peaks in the HV-TER spectrum. To explore the origin of additional vibrational peaks, IR vibrational spectrum of pyrazine powder was also measured, and compared with the HV-TER spectra, which demonstrate that some of the strongly enhanced vibrational peaks are IR-activated modes of pyrazine.

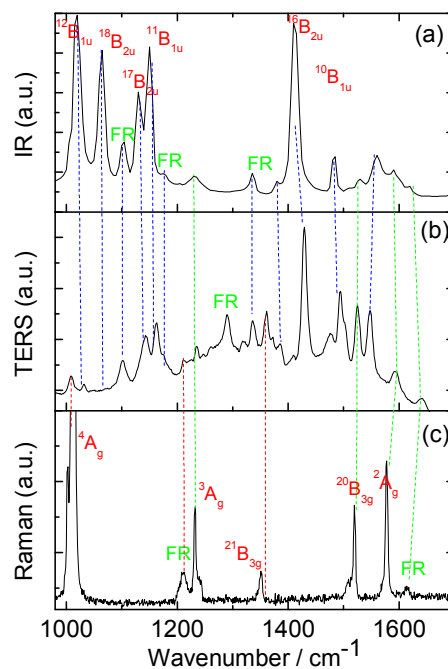


Figure 8. Vibrational spectra of pyrazine. (a) The measured IR vibrational spectrum of pyrazine powder. (b) The HV-TERS spectra of pyrazine adsorbed on Ag the film. (c) The Raman spectrum of pyrazine powder. Figure 8 is taken from Ref. [4].

The near field gradient effect has also been observed in Raman spectra of DMAB adsorbed on Au film in HV-TERS.¹⁰ The HV-TERS spectrum of DMAB adsorbed on gold film is shown in Fig. 9a. Fig. 9b and 9c are the measured Raman spectra of DMAB powder, and Fig. 9c is IR vibrational spectrum of DMAB. Comparing Fig. 9a with Fig. 9b and 9c, one can find that the Raman and IR-active modes of DMAB in HV-TERS spectrum can be very clearly observed.

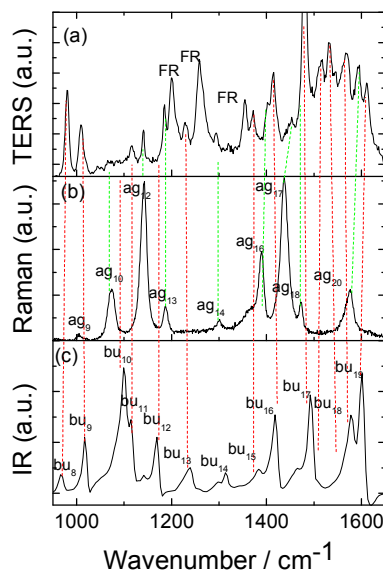


Figure 9. (a) The TER spectrum of DMAB adsorbed on the gold film. (b) Raman spectrum of DMAB powder. (c) The IR vibrational spectrum of DMAB. Figure 9 is taken from Ref. [10].

The IR vibrational modes of DMAB produced from 4NBT and PATP were also observed experimentally by two different groups,^{10, 33} as shown in Fig. 10 and 11. The 4NBT and PATP were different, but their TER spectra were very similar, which further confirms that the TER spectra are the Raman spectra of DMAB produced from 4NBT and PATP, respectively, and were theoretically confirmed in Ref.¹⁰. Note that Fig. 11 was measured in 2010, and it was interpreted with chemical enhancement.³³ The latest experimental and theoretical results revealed that PATP was catalyzed to DMAB through a plasmon-driven reaction.¹⁰

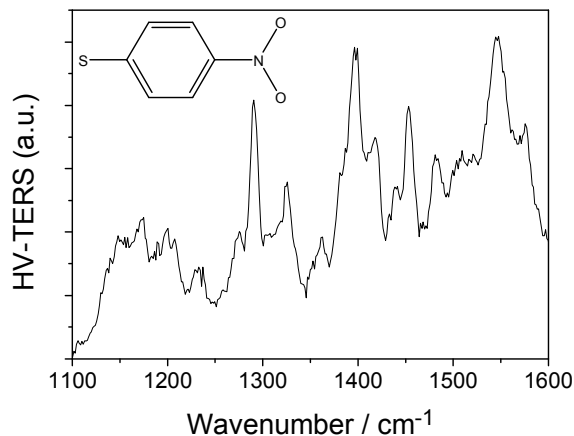


Figure 10. TER spectrum of DMAB produced from 4NBT. Figure 10 is taken from Ref. [10].

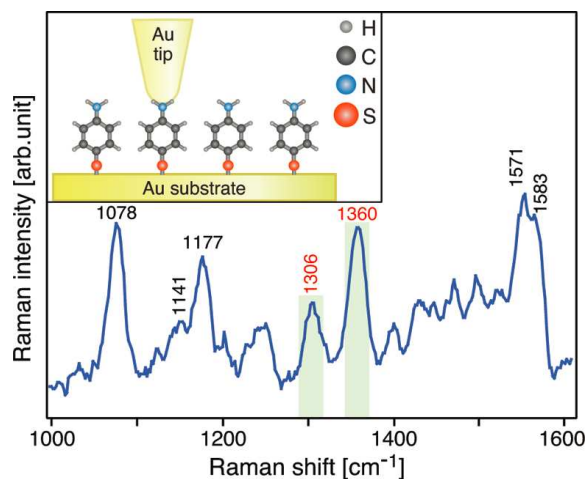


Figure 11. TER spectrum of DMAB produced from PATP molecules sandwiched between Au substrate and Au tip, as illustrated in the inset. Figure 11 is taken from Ref. [33].

4.2 Overtone and combinational modes in HV-TERS

In the theory of second-order perturbation, the diagonal matrix element of Eq. 1 includes contributions to harmonic and anharmonic terms,

$$\langle v_i | H_{vib}^{eff} | v_i \rangle = \sum_r \omega_r \left(n_r + \frac{1}{2} \right) + \sum_{r < s} x_{rs} \left(n_r + \frac{1}{2} \right) \left(n_s + \frac{1}{2} \right) + \dots \quad (6)$$

where ω_r is harmonic frequency for the mode r , n_r is the vibrational quantum number, and x_{rs} is anharmonic coupling constant between modes s and r . Here, it is restricted the analysis of two resonant effects to those off-diagonal matrix elements for the Fermi resonance^{45, 52} and the Darling-Dennison resonance^{46, 53} which are written as,

$$\langle v_r + 1, v_s + 1, v_t | H_{vib}^{eff} | v_r, v_s, v_t + 1 \rangle = \frac{k_{rst}}{2} \sqrt{\frac{(v_r + 1)(v_s + 1)(v_t + 1)}{2}} \quad (7)$$

$$\langle v_r + 2, v_t | H_{vib}^{eff} | v_r, v_t + 1 \rangle = \frac{k_{rrt}}{4} \sqrt{\frac{(v_r + 2)(v_r + 1)(v_t + 1)}{2}} \quad (8)$$

$$\langle v_r + 2, v_t | H_{vib}^{eff} | v_r, v_t + 2 \rangle = \frac{k_{rrt}}{4} \sqrt{(v_r + 1)(v_r + 2)(v_t + 1)(v_t + 2)} \quad (9)$$

Equations (7) and (8) are the Fermi resonance for the combinational and overtone modes, respectively. Eq. (5) is Darling-Dennison resonance for the first overtone modes,

where k_{rst} , k_{rrt} and k_{rrt} are three anharmonic force constants. Their operators in Eqs.(7) - (9) can be written as,

$$V_{rst(rrt)}^{Fermi} = k_{rst(rrt)} a_r^+ a_{s(r)} a_t + \text{Hermitian conjugate} \quad (10)$$

$$V_{rrt}^{DD} = k_{rrt} a_r^+ a_r^+ a_t a_t + \text{Hermitian conjugate} \quad (11)$$

In Eqs. (10) and (11), a^+ and a are raising and lowering operators, respectively.

4.2.1 Fermi resonances in HV-TERS

The Fermi resonances have been experimentally observed in the plasmon-driven catalytic reaction of DMAB produced from PATP adsorbed on Au film, revealed by HV-TER spectra.⁴⁵ For the Fermi resonance, the splitting of two vibrational energies under perturbations can be written as [^{45, 52}],

$$E_{\pm} = \frac{1}{2}(E_A + E_B) \pm \frac{1}{2}\sqrt{(E_A - E_B)^2 + 4\phi^2} \quad (12)$$

where E_A and E_B are vibrational energies of the fundamental mode and an overtone of a different fundamental mode (or a combination mode) before splitting, ϕ is the Fermi Resonance coupling coefficient, which describes the coupling strength of the fundamental vibrational mode and the combinational mode (or the overtone mode) in the Fermi Resonance. According to the splitted peaks, these two unperturbed energies E_A and E_B can be estimated as

$$E_A = \frac{E_+ + E_-}{2} + \frac{E_+ - E_-}{2} \times \frac{I_+ - I_-}{I_+ + I_-} \quad (13)$$

$$E_B = \frac{E_+ + E_-}{2} - \frac{E_+ - E_-}{2} \times \frac{I_+ - I_-}{I_+ + I_-} \quad (14)$$

where I_+ and I_- are Raman intensities of these two splitted peaks. The energy difference between the perturbed levels in the presence and absence of Fermi Resonance can be well estimated with $\Delta E_{\pm} = E_+ - E_-$ and $\Delta E_{AB} = |E_A - E_B|$, respectively.

Using above formulas, one can obtain $I_+(ag_{13}) \approx I_-(g_{13})$ and $I_+(bu_{13}) \approx \frac{1}{2}I_-(bu_{13})$, and also $\Delta E_{\pm}(ag_{13}) = 20.4 \text{ cm}^{-1}$ as well as $\Delta E_{\pm}(bu_{13}) = 14.6 \text{ cm}^{-1}$ in Fig.12a. According to Eqs. 13 and 14, for the Raman-active (symmetric mode) ag_{13} , one can obtain $E_A = E_B = \frac{E_+ + E_-}{2}$, i.e. $\Delta E_{AB} \approx 0 \text{ cm}^{-1}$, and Fermi Resonance coupling coefficient (calculated by using Eq. 12) is $\phi(ag_{13}) = \frac{1}{2}\Delta E_{\pm}(ag_{13}) = 10.2 \text{ cm}^{-1}$. Fig. 12b and 12c illustrate different vibrational modes which are marked with short vertical lines, the fundamental Raman-active (symmetric mode) ag_{13} frequency at 1213 cm^{-1} is very close to the frequency of combinational mode of ag_6 at 727 cm^{-1} and bg_6 at 485 cm^{-1} , which is $\Delta E_{AB} = E(ag_{13}) - [E(bg_6) + E(ag_6)] \approx 1 \text{ cm}^{-1}$. The combinational mode is asymmetric, because of $bg \times ag = bg$.

For the IR-active (asymmetric mode) bu_{13} , one can obtain $E_A = \frac{E_+ + E_-}{2} + \frac{1}{3} \times \frac{\Delta E_{\pm}}{2}$ and $E_B = \frac{E_+ + E_-}{2} - \frac{1}{3} \times \frac{\Delta E_{\pm}}{2}$, using Eqs. 13, Eqs. 14, and $I_+(bu_{13}) \approx \frac{1}{2}I_-(bu_{13})$ (see Fig. 13(a)). And then $\Delta E_{AB}(bu_{13}) = \frac{1}{3}\Delta E_{\pm}(bu_{13}) = 4.9 \text{ cm}^{-1}$ as well as $\phi(bu_{13}) = \frac{\sqrt{2}}{3}\Delta E_{\pm}(bu_{13}) = 6.88 \text{ cm}^{-1}$ can be obtained as well, respectively. The calculated IR-active asymmetric bu_{13} mode frequency at 1267 cm^{-1} is about 7 cm^{-1} smaller than the combinational mode of bu_5 at 634 cm^{-1} and bu_6 at 640 cm^{-1} . The difference between the theoretical and experimental values (7 cm^{-1} and 4.9 cm^{-1}) is about 2 cm^{-1} . The symmetry of the combinational mode is symmetric, because of $bu \times bu = ag$.

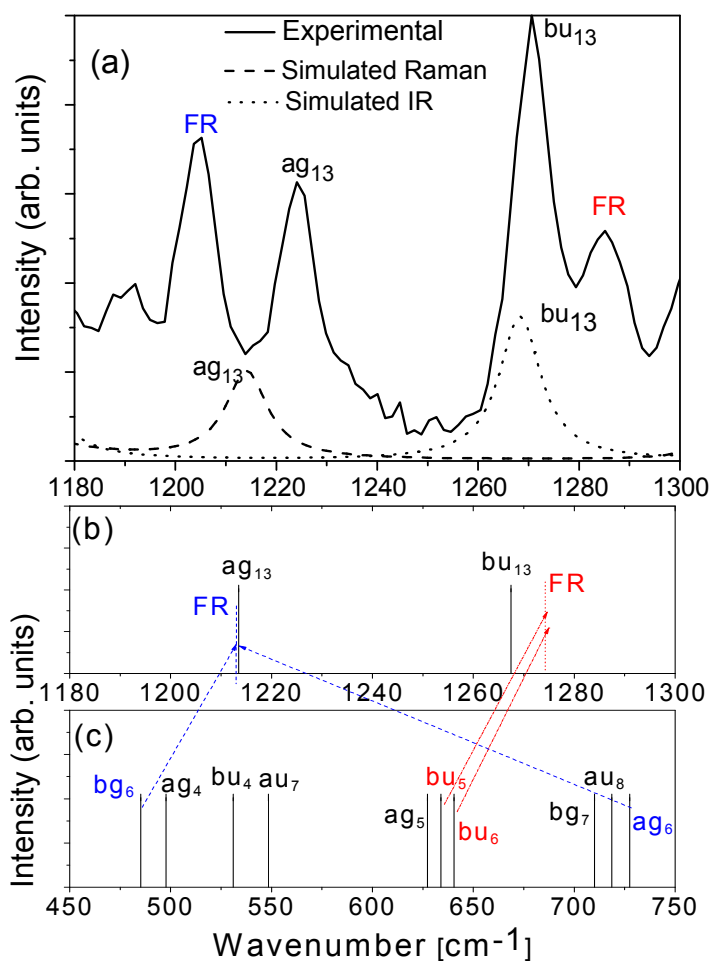


Figure 12. (a) The experimentally Fermi resonance and simulated TER spectra of DMAB for Raman-active ag_{13} and IR-active bu_{13} modes. (b) and (c) The calculated vibrational modes and the combinational modes for Fermi resonance. Figure 12 is taken from Ref. [45].

4.2.2 Darling–Dennison resonance in HV-TERS

The Darling–Dennison resonance is the first overtone- resonant interaction (1:1 resonance coupling), and these two resonant first overtones are presented in HV-TERS. Figure 13a demonstrates HV-TER spectra of thiourea adsorbed on the Ag film, and one can see that there are five strong Raman peaks. However, the measured normal Raman scattering spectra (see Fig. 13b) of thiourea powder shows there is no any Raman peaks in these regions. So the experimental five Raman peaks should not result from the fundamental frequency vibrational modes. The measured Raman peaks are mainly attributed to thiourea in the thione form. The simulations of the thiourea (in the thione

form) adsorbed on the Ag₂₀ cluster shown that there is not any normal mode in these regions from 800 cm⁻¹ to 1050 cm⁻¹ (see Fig. 13c). It should be noticed that there is not any Raman peak in the region of 600-700 cm⁻¹ in measured Raman spectrum in the Fig. 13b, but the simulated Raman spectrum revealed that there are two weak Raman peaks in the region (Fig. 13c). These two Raman peaks are too weak to be clearly observed experimentally; but the interaction between molecules and the metal results in the enhancement of these two Raman peaks (mode e and mode f in the Fig. 13c). These vibrational modes e and f, as well as the interaction between molecules and metal are shown in Fig. 13e.

The Darling–Dennison resonance enhanced by tip can be well used to explain above four modes of five peaks. Peak A and B in Fig.13a are two perturbed first overtone modes (resonant interaction), and their perturbed foundational modes *a* and *b* can be clearly seen in the Fig. 13c. Similarly, Peak C and D in Fig. 13a are two perturbed first overtone modes (resonant interaction), and the perturbed foundational modes *c* and *d* can be seen clearly in Fig. 13c as well. Their vibrational modes are shown in Fig. 13e. It should be noted that Darling–Dennison resonance cannot be observed in traditional SERS experiment (Fig. 13d). The peak E in Fig. 13a is the combinational mode of modes *c* and *d*. To further confirm that, the SERS of thiourea molecule adsorbed on the Ag film were measured, and this Raman peak can also be clearly found in Fig. 13d. The slight shift of peak E between SERS and TERS may result from influence of the tip. In the SERS spectra, the peak E is hardly to be interpreted using combinational modes, because there is neither perturbed fundamental Raman peak for Fermi Resonance, nor the perturbed overtone modes for the Darling–Dennison resonance (where Darling–Dennison resonance in SERS is too weak to be observed).

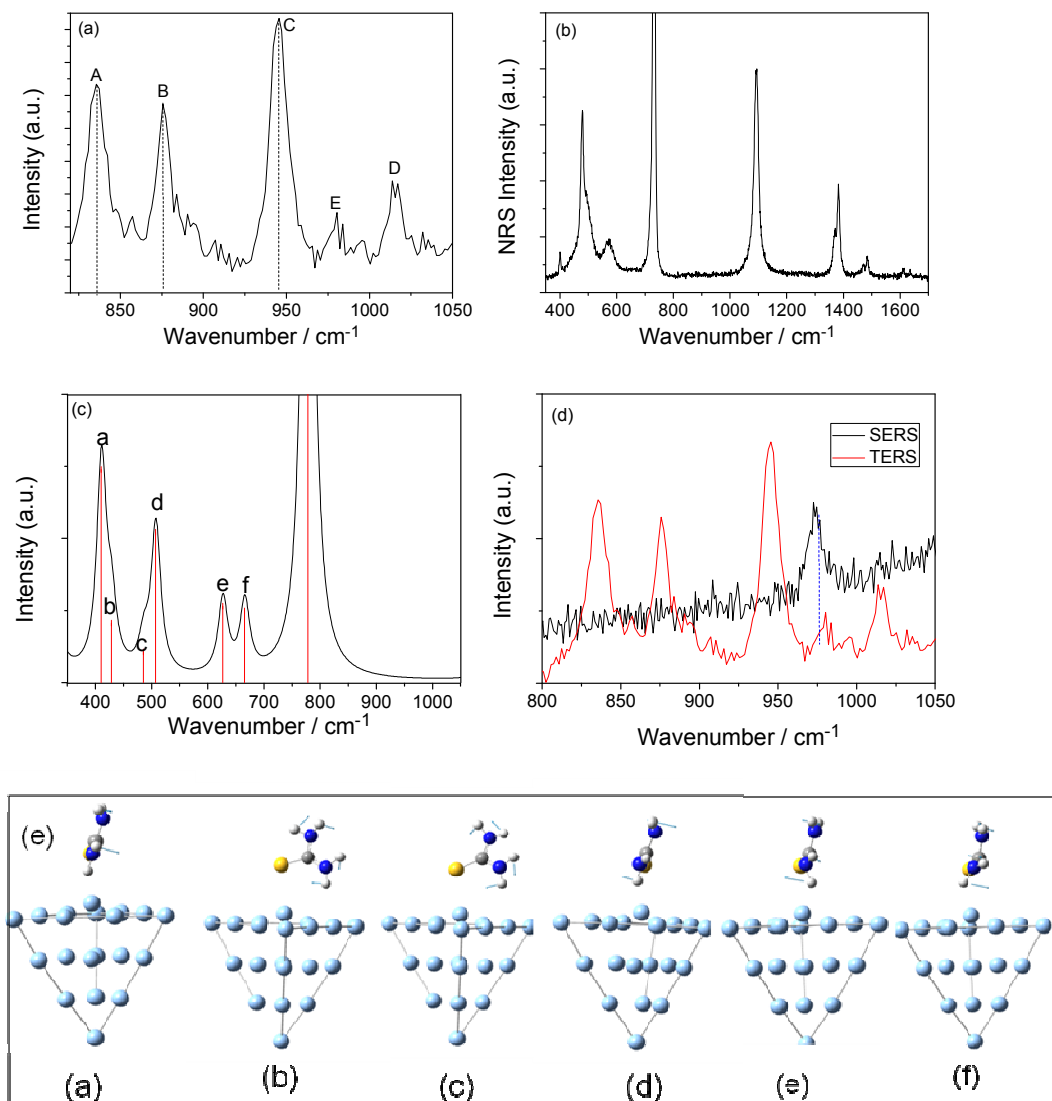


Figure 13. (a) TER spectra in the region from 800 to 1050 cm^{-1} . (b) The measured Raman spectra of the thiourea powder (c) The calculated Raman spectra of thiourea adsorbed on the Ag_{20} cluster in the thione form (d) The measured TER and SERS spectra from 800 to 1050 cm^{-1} (e) The calculated vibrational modes. Figure 13 is taken from Ref. [46].

4.3 Chemical mapping of a single molecule by plasmon-enhanced Raman scattering

Thanks to the strong electric field and sharp gradient field yielded by the tip-substrate cavity plasmon, nanoscale TER imaging and single molecule resolved TER spectra could be easily obtained.^{5, 8, 22} Additionally, it allows for non-invasive single

molecule sensitivity TERS measurements and explores the influence of molecular orientations on the vibrational spectral features. Fig. 14a shows two representative TERS spectra of two molecules with different tilted angle as they are on an atomic stage as shown in the STM images on the right. Both spectra reveal the vibrational features of molecules, but with different relative peak intensity. The calculation by a DFT under dipole approximation of the molecules shows the particular orientation of the molecules (see Fig. 14b). It is found that when the molecules flatly adsorbed on the substrate, the IR-active mode (indicated with red line) are strong.⁵⁴ When the tilt angle is 30°, the Raman intensities significantly increase, but the IR-active modes relatively decrease. The reason is that the linear plasmon intensity is significantly enhanced, while the ratio of plasmonic gradient effect decreases when the molecule tilt is 30°, compared that molecule flatly adsorbed on the substrate.⁵⁴

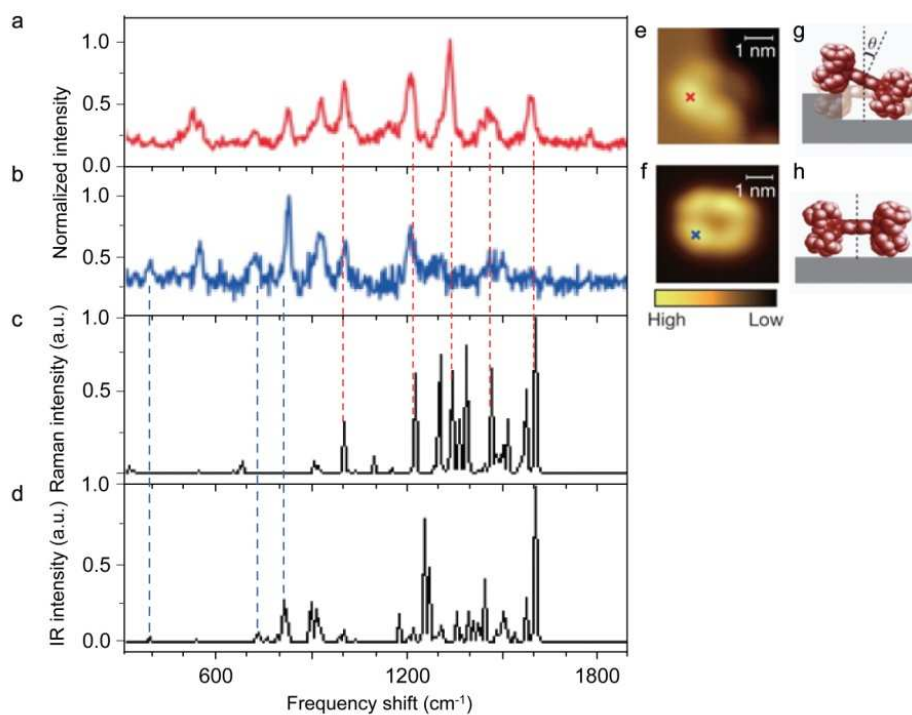


Figure 14 (a) and (b) Single-molecule TERS spectra for an isolated H₂TBPP molecule adsorbed on the terrace or at the step edge. (c) and (d) Calculated TERS spectra of H₂TBPP. (e) and (g) STM image and schematic image of H₂TBPP molecule flatly adsorbed on Ag substrate. (f) and (h) STM image and schematic image of tilted H₂TBPP molecule with tilt angle of 30°. Figure 14 is taken from Ref. [8].

V. Conclusion and Prospective

The principle of plasmonic gradient effect in HV-TERS has been interpreted using electromagnetic field gradient theory, which revealed that plasmonic gradient is strongly dependent on the gap distance in near field. The near field plasmonic gradient effects can activate IR vibrational modes, which makes the Raman selection rules broken. Thus, in the near field, the Raman and IR vibrational modes can be simultaneously observed in HV-TERS, which is so-called “complete (3N-6 modes)” vibration spectra.

The atomic-resolution measurements as well as structural elucidation for molecules adsorbed on the substrate can be obtained by HV-STM-TERS on the clean, single-crystal and/or nanostructured surfaces at low temperature. The *in-situ* topographical imaging and spectra can be simultaneously obtained, which provide ideal techniques for revealing the nature of plasmon-driven chemical reactions. Further improvements, including femtosecond lasers for the time-resolved UHV-STM-TERS spectra, are the most important part in the investigation of surface molecular catalysis reaction dynamics in future experimental works.

Acknowledgements: This work was supported by the National Natural Science Foundation of China (91436102, 11374353 and 11474141). Y. Fang would like to thank Prof. M. Käll for stimulating discussion and the Kunt and Alice Wallenberg Foundation for financial support. Z. Zhang thanks the support from the Alexander von Humboldt foundation.

References:

1. N. Mauser and A. Hartschuh, *Chem. Soc. Rev.*, 2014, 43, 1248-1262.
2. Z. L. Zhang, S. X. Sheng, H. R. Zheng, H. X. Xu and M. T. Sun, *Nanoscale*, 2014, 6, 4903-4908.
3. M. Sun, Z. Zhang, L. Chen, Q. Li, S. Sheng, H. Xu and P. Song, *Adv. Mater. Interf.*, 2014, 1, 2196-7350.
4. M. T. Sun, Z. L. Zhang, L. Chen, S. X. Sheng and H. X. Xu, *Adv. Opt. Mater.*, 2014, 2, 74-80.
5. M. D. Sonntag, D. Chulhai, T. Seideman, L. Jensen and R. P. Van Duyne, *J. Am. Chem. Soc.*, 2013, 135, 17187-17192.
6. M. Paulite, C. Blum, T. Schmid, L. Opilik, K. Eyer, G. C. Walker and R. Zenobi, *Acs Nano*, 2013, 7, 911-920.
7. T. Schmid, L. Opilik, C. Blum and R. Zenobi, *Angew. Chem. Int. Edit.*, 2013, 52, 5940-5954.

8. R. Zhang, Y. Zhang, Z. C. Dong, S. Jiang, C. Zhang, L. G. Chen, L. Zhang, Y. Liao, J. Aizpurua, Y. Luo, J. L. Yang and J. G. Hou, *Nature*, 2013, 498, 82-86.
9. M. T. Sun, Z. L. Zhang, Z. H. Kim, H. R. Zheng and H. X. Xu, *Chem-Eur. J.*, 2013, 19, 14958-14962.
10. Z. L. Zhang, M. T. Sun, P. P. Ruan, H. R. Zheng and H. X. Xu, *Nanoscale*, 2013, 5, 4151-4155.
11. Z. L. Zhang, L. Chen, M. T. Sun, P. P. Ruan, H. R. Zheng and H. X. Xu, *Nanoscale*, 2013, 5, 3249-3252.
12. R. M. Stockle, Y. D. Suh, V. Deckert and R. Zenobi, *Chem. Phys. Lett.*, 2000, 318, 131-136.
13. M. S. Anderson, *Appl. Phys. Lett.*, 2000, 76, 3130-3132.
14. N. Hayazawa, Y. Inouye, Z. Sekkat and S. Kawata, *Opt. Commun.*, 2000, 183, 333-336.
15. B. Pettinger, G. Picardi, R. Schuster and G. Ertl, *J. Electroanal. Chem.*, 2003, 554, 293-299.
16. B. Pettinger, B. Ren, G. Picardi, R. Schuster and G. Ertl, *Phys. Rev. Lett.*, 2004, 92.
17. B. Ren, G. Picardi and B. Pettinger, *Rev. Sci. Instrum.*, 2004, 75, 837-841.
18. N. Anderson, A. Hartschuh, S. Cronin and L. Novotny, *J. Am. Chem. Soc.*, 2005, 127, 2533-2537.
19. K. F. Domke, D. Zhang and B. Pettinger, *J. Am. Chem. Soc.*, 2006, 128, 14721-14727.
20. W. H. Zhang, X. D. Cui, B. S. Yeo, T. Schmid, C. Hafner and R. Zenobi, *Nano Lett.*, 2007, 7, 1401-1405.
21. J. Steidtner and B. Pettinger, *Rev. Sci. Instrum.*, 2007, 78, 103104.
22. J. Steidtner and B. Pettinger, *Phys. Rev. Lett.*, 2008, 100, 236101.
23. E. Bailo and V. Deckert, *Chem. Soc. Rev.*, 2008, 37, 921-930.
24. A. Hartschuh, N. Anderson and L. Novotny, *J. Microsc-Oxford*, 2003, 210, 234-240.
25. J. N. Chen, W. S. Yang, K. Dick, K. Deppert, H. Q. Xu, L. Samuelson and H. X. Xu, *Appl. Phys. Lett.*, 2008, 92, 093110.
26. M. T. Sun, Y. R. Fang, Z. L. Yang and H. X. Xu, *Phys. Chem. Chem. Phys.*, 2009, 11, 9412-9419.
27. T. Yano, P. Verma, Y. Saito, T. Ichimura and S. Kawata, *Nat. Photonics*, 2009, 3, 473-477.
28. D. Zhang, U. Heinemeyer, C. Stanciu, M. Sackrow, K. Braun, L. E. Hennemann, X. Wang, R. Scholz, F. Schreiber and A. J. Meixner, *Phys. Rev. Lett.*, 2010, 104, 056601.
29. J. Stadler, T. Schmid and R. Zenobi, *Nano Lett.*, 2010, 10, 4514-4520.
30. Y. R. Fang, W. S. Yang, S. Fang and H. X. Xu, *China Pat.*, CN101915756A, 2010.
31. K. F. Domke and B. Pettinger, *Chemphyschem*, 2010, 11, 1365-1373.
32. H. Kim, K. M. Kosuda, R. P. Van Duyne and P. C. Stair, *Chem. Soc. Rev.*, 2010, 39, 4820-4844.

33. K. Uetsuki, P. Verma, T. Yano, Y. Saito, T. Ichimura and S. Kawata, *J. Phys. Chem. C*, 2010, 114, 7515-7520.
34. T. Deckert-Gaudig, E. Rauls and V. Deckert, *J. Phys. Chem. C*, 2010, 114, 7412-7420.
35. B. R. Wood, E. Bailo, M. A. Khiavi, L. Tilley, S. Deed, T. Deckert-Gaudig, D. McNaughton and V. Deckert, *Nano Lett.*, 2011, 11, 1868-1873.
36. Z. L. Yang, Q. H. Li, Y. R. Fang and M. T. Sun, *Chem. Commun.*, 2011, 47, 9131-9133.
37. M. T. Sun, Z. L. Zhang, H. R. Zheng and H. X. Xu, *Sci. Rep.*, 2012, 2, 647.
38. N. Jiang, E. T. Foley, J. M. Klingsporn, M. D. Sonntag, N. A. Valley, J. A. Dieringer, T. Seideman, G. C. Schatz, M. C. Hersam and R. P. Van Duyne, *Nano Lett.*, 2012, 12, 5061-5067.
39. E. M. van Schrojenstein Lantman, T. Deckert-Gaudig, A. J. G. Mank, V. Deckert and B. M. Weckhuysen, *Nat. Nanotechnol.*, 2012, 7, 583-586.
40. N. Kazemi-Zanjani, H. H. Chen, H. A. Goldberg, G. K. Hunter, B. Grohe and F. Lagugne-Labarthe, *J. Am. Chem. Soc.*, 2012, 134, 17076-17082.
41. D. Kuroski, T. Deckert-Gaudig, V. Deckert and I. K. Lednev, *J. Am. Chem. Soc.*, 2012, 134, 13323-13329.
42. B. Pettinger, P. Schambach, C. J. Villagomez and N. Scott, *Annu. Rev. Phys. Chem.*, Vol 63, 2012, 63, 379-399.
43. J. Stadler, T. Schmid and R. Zenobi, *Nanoscale*, 2012, 4, 1856-1870.
44. M. D. Sonntag, J. M. Klingsporn, L. K. Garibay, J. M. Roberts, J. A. Dieringer, T. Seideman, K. A. Scheidt, L. Jensen, G. C. Schatz and R. P. Van Duyne, *J. Phys. Chem. C*, 2012, 116, 478-483.
45. M. Sun, Y. Fang, Z. Zhang and H. Xu, *Phys. Rev. E*, 2013, 87, 020401.
46. M. T. Sun, Z. L. Zhang, L. Chen and H. X. Xu, *Adv. Opt. Mater.*, 2013, 1, 449-455.
47. M. Tabatabaei, A. Sangar, N. Kazemi-Zanjani, P. Torchio, A. Merlen and F. Lagugne-Labarthe, *J. Phys. Chem. C*, 2013, 117, 14778-14786.
48. E. J. Ayars, H. D. Hallen and C. L. Jahncke, *Phys. Rev. Lett.*, 2000, 85, 4180-4183.
49. E. J. Ayars, H. D. Hallen and M. A. Paesler, *Abstr. Pap. Am. Chem. S*, 2001, 221, U96-U96.
50. A. D. Buckingham, in *Advances in Chemical Physics*, John Wiley & Sons, Inc., 2007, DOI: 10.1002/9780470143582.ch2, pp. 107-142.
51. A. D. Buckingham, *Adv. Chem. Phys.*, 1967, 12, 107.
52. E. Fermi, *Z. Physik*, 1931, 71, 250-259.
53. B. T. Darling and D. M. Dennison, *Phys. Rev.*, 1940, 57, 128-139.
54. L. Y. Meng, Z. L. Yang, J. N. Chen and M. T. Sun, in preparation.